

# PREPRINT - Controlling a Solar Receiver with Multiple Thermochemical Reactors for Hydrogen Production by an LSTM Neural Network based Cascade Controller

Laurin Oberkirsch<sup>a,\*</sup>, Johannes Grobbel<sup>b</sup>, Daniel Maldonado Quinto<sup>a</sup>, Peter Schwarzbözl<sup>a</sup>, Bernhard Hoffschmidt<sup>a</sup>

<sup>a</sup>German Aerospace Center (DLR), Institute of Solar Research, Linder Höhe, D-51147 Köln, Germany

<sup>b</sup>German Aerospace Center (DLR), Institute of Future Fuels, Professor-Rehm-Straße 1, 52428 Jülich, Germany

---

## Abstract

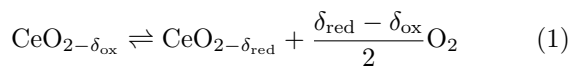
Solar reactors for batch processes have a varying heat demand over time. The receiver of large-scale solar chemical plants consists of several of these reactors to quasi-continuously use the solar resource. For this, the heliostat field needs to provide a non-uniform time-varying flux density distribution. As this differs from the heliostat field control of a typical CSP plant, it challenges its control. Here, we propose a cascade controller for a coupled system of heliostat field and receiver consisting of 19 thermochemical batch reactors for hydrogen generation. In the receiver controller, a fast long short-term memory (LSTM) neural network model predicts the future temperatures and the ceria reduction extends in the reactors as a function of the flux density. It is trained with data from a thermochemical reactor model. The trained LSTM neural network is embedded in a hybrid automaton to model the continuous batch process states. Discrete state changes are made when certain conditions are reached. In this way, the receiver controller determines flux density setpoints leading to high efficiencies for each reactor. The heliostat field controller applies aim point optimization to provide flux densities close to these setpoints. With this cascade control, reactor array efficiencies of 79% are obtained. Moreover, the individual reactors operate within their material limits and come close to their optimal efficiency. In addition, it is found that secondary concentrators complicate the control and decrease the reactor array efficiency. However, they still increase the overall efficiency by 51.3% due to a significantly higher optical efficiency.

*Keywords:* concentrating solar power, solar tower, solar thermochemical water splitting, hydrogen generation, aim point optimization, LSTM neural network

---

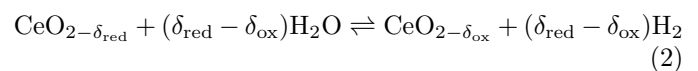
## 1. Introduction

Hydrogen is considered to play a key role in reducing green house gas emissions of various industries and sectors in the future (International Energy Agency, 2019). This is only possible if the hydrogen itself is produced with low emissions. One production path are solar thermochemical redox cycles, which exhibit a high theoretical efficiency (Nakamura, 1977) and are subject of ongoing research. In these cycles, a redox material is reduced in a first step at high temperatures of about 1400 °C by means of concentrated solar energy. Equation 1 describes the reduction of ceria, a popular redox material used for these cycles.



The reduction extent after reduction and oxidation is denoted with  $\delta_{\text{red}}$  and  $\delta_{\text{ox}}$ , respectively. To obtain a high reduction extent, the oxygen partial pressure is usually kept low by purging with an inert gas (Roeb et al., 2011),

by reducing the overall pressure with vacuum pumps (Ermamoski et al., 2013; Singh et al., 2017) or by a combination of both (Marxer et al., 2017). In a second step, the reduced oxide is oxidized with steam at lower temperatures of about 900 °C so that hydrogen is generated as it is stated for ceria in equation 2. Alternatively, syngas can be produced by introducing carbon dioxide as a second oxidator.



For the reduction of the redox material, various solar reactor designs have been proposed (Agrafiotis et al., 2015). They can be classified into continuously irradiated reactors with moving redox material in the form of porous structures (Diver et al., 2010; Falter et al., 2015; Brendelberger et al., 2022) or particles (Singh et al., 2017) and in discontinuously irradiated reactors with fixed redox material, also in the form of porous structures (Säck et al., 2016; Marxer et al., 2017) or particles (Yang et al., 2021). The latter reactor type with a directly irradiated redox material in form of a fixed reticulated porous ceramic was demonstrated in largest scale (Säck et al., 2016) and is the one with highest demonstrated efficiency (Marxer et al.,

---

\*Corresponding author

Email address: laurin.oberkirsch@dlr.de (Laurin Oberkirsch)

## Nomenclature

$A$	Aperture area, [m]	$\delta$	Level of ceria reduction
$D_h$	Heliostat distance, [m]	$\delta_S$	Angular sun diameter
$T$	Maximum temperature of the absorber, [K]	$\eta_{\text{array}}$	Array efficiency
$\bar{n}_{\text{H}_2}^{\text{out}}$	Molar flow of hydrogen, [mol s <sup>-1</sup> ]	$\eta_{\text{combined}}$	Combined efficiency
$\mathbf{y}$	Flux density distribution, [W m <sup>-2</sup> ]	$\eta_{\text{non-centered}}$	Non-centered aiming efficiency
$\dot{q}_{\text{rad}}''$	Flux density, [W m <sup>-2</sup> ]	$\eta_{\text{optical}}$	Optical efficiency
$d$	Receiver diameter, [m]	$\eta_{\text{reactor,current}}$	Current reactor efficiency
$f_{\text{reactor,current}}$	Factor for current reactor efficiency, [m <sup>2</sup> W <sup>-1</sup> ]	$\eta_{\text{reactor}}$	Reactor efficiency
$i$	Index	$AFD$	Allowed flux density
$max$	Maximum	$BPTT$	Backpropagation through time
$ox$	Oxidation	$CSP$	Concentrated solar power
$red$	Reduction	$HHV$	Higher heating value
$set$	Setpoint	$J$	Objective function
$t$	Time	$LSTM$	Long short-term memory
$\Delta\delta$	Change in the level of ceria reduction	$MAE$	Mean absolute error
		$RMSE$	Root-mean-square error
		$TBPTT$	Truncated backpropagation through time

2017). Figure 2 shows a schematic of the design used in the HYDROSOL project series (Säck et al., 2016).

A reactor of this type is operated in batch mode and its operation should be investigated in the current study. As the oxidation and reduction reactions take place in the same location and gas flow can hardly be used for temperature control (Roca et al., 2013; Säck et al., 2015), the concentrated solar radiation entering the reactor needs to be controlled to reach the required temperatures for the reactions.

There have been only a few studies on the control of these solar batch reactors. Roca et al. (2013) proposed a PI control with adaptive gain scheduling for the temperature control. Säck et al. (2016) also control the temperature in the reactor with a PI controller. Specific groups of heliostats within the respective group are focused or defocused if a certain tolerance limit is exceeded. As an improvement to their first study, Roca et al. (2016) applied a feed forward Knapsack controller in combination with a PI controller.

These studies obtained good results: the temperature in the reactors could be controlled well, even when some weather disturbances were present (Roca et al., 2016; Säck et al., 2016). However, even though a two-reactor system was investigated, there was no interdependency between reactors as for each reactor a dedicated portion of the field was reserved and only one reactor was irradiated at once. Also, the duration of oxidation and reduction phases is set to a fixed value of 30 minutes in these studies. The temperature setpoints are also prescribed.

In further studies, a four reactor-system is recommended

to maximize the net receiver power (Li et al., 2020a) and a beam-down optical system with a rotating tower reflector is proposed to alternate the irradiation between the reactors of an array (Li et al., 2020b; Yang et al., 2021). At commercial-size solar towers, multiple arrays of reactors are foreseen (Schäppi et al., 2022). The first study dealing with arrays of reactors was performed by Brendelberger et al. (2020), who investigated the operation of three arrays. The reactors are only irradiated during reduction and only one array is irradiated at once. The reduction phase of an array runs until the material limit (in this case set to 2100 K) is reached in one of the reactors of the array. Then, the next array is irradiated, which means that the reduction duration must be one third of the total cycle duration and that many reactors in the array do not reach the targeted maximum temperature.

In another study, Grobbel et al. (2022) developed a heuristic approach for the operation of a single array with multiple reactors. For a number of radiative fluxes at the aperture, optimal periods of reduction and oxidation were determined for a single reactor. Then, the heuristic distributes the concentrated solar power to each reactor, runs each of them with the optimal reduction and oxidation duration for a single reactor and shifts the processes in between the reactors so that only little power is wasted. The approach has some limitations though: For each reactor, the heat flux at the aperture is fixed even though it is influenced by spillage from irradiating other reactors or by weather. It was also shown that a variable heat flux to a single reactor can increase its efficiency but it can hardly be used in an array operated with the heuristic approach of Grobbel et al. (2022).

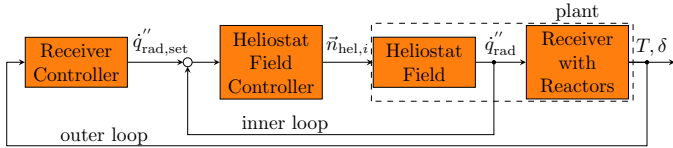


Figure 1: Overview over the cascade control comprising outer and inner control loop. The inner heliostat field control loop is fast and exhibits only little dynamics, while the outer receiver control loop is highly dynamic. The heliostat field controller controls the flux density radiating in each reactor, whereas the receiver controller controls the temperatures to achieve high reactor efficiencies.

In solar tower systems, deep learning has already been applied in multiple areas such as solar tracking systems (Carballo et al., 2019), heliostat tracking (Carballo et al., 2020), heliostat calibration (Pargmann et al., 2021), thermal power forecasting (Wang et al., 2020) or aiming strategy optimization (Zeng et al., 2022).

In this work, we present a cascade control for a receiver with multiple reactors, each modeled by a *Long Short-Term Memory* (LSTM) neural network. It has neither the limitation of fixed cycle duration nor the limitation of prescribed fluxes or target temperatures in the individual reactors. This is made possible by coupling the control of the reactors with the control of the heliostat field. The control is demonstrated on a receiver with 19 reactors, once with and once without secondary concentrators. The results are discussed and compared to other control approaches.

## 2. Methods

### 2.1. Cascade control

The system to be controlled comprises the heliostat field and the receiver with its 19 individual reactors. Thus, it covers the optical as well as the thermochemical part of the system. The aim of this work is to develop a control that operates all reactors safely below the material limit of 2000 K while reaching a high total hydrogen production of all reactors  $\bar{n}_{\text{H}_2,\text{total}}^{\text{out}}$ .

The thermochemical subsystem includes strong dynamics with heating, cooling, reduction and oxidation periods of several minutes. In contrast, the optical subsystem exhibits less dynamics as the heliostats move within seconds and provide a completely altered flux density distribution. Thus, a cascade control as visualized in figure 1 is perfectly suited to control the entire system.

A receiver controller determines flux density setpoints for each reactor  $q''_{\text{rad,set},i}$  in an outer control loop and transfers them towards the inner heliostat field control loop. Within the heliostat field control loop, aim point optimization is applied to identify optimal aim point distributions. A single aim point optimization requires roughly two seconds and needs to be repeated each time the setpoint flux of one reactors varies. By assigning the heliostats to specific aim points (reactors), the heliostat field delivers a flux for each reactor  $q''_{\text{rad},i}$  on the receiver. In this study, the

heliostat field is modeled by a raytracer. At a real plant, a closed-loop heliostat field control would compensate for errors in the simulation model, e.g. incorrectly modeled tracking errors. This study assumes the simulation model to be perfect so that no inner feedback loop is required. Based on the simulated fluxes, each reactor model calculates its virtual hydrogen output  $\bar{n}_{\text{H}_2,i}^{\text{out}}$ .

The aim of the receiver controller is to maximize the hydrogen output while keeping the maximum reactor temperature below the material limit. Instead of controlling the hydrogen output directly, the change in the level of ceria reduction of each individual reactor is used as control variable. The advantage of the level of ceria reduction  $\delta$  compared to the hydrogen output is that it varies both during reduction and during oxidation. The larger the change in reduction extent, the more hydrogen is produced. Thus, it simplifies the control while providing the control with enough information.

The receiver inputs are the flux density  $q''_{\text{rad},i}$ , the mass flow of the flushing gas nitrogen  $\dot{m}_{\text{N}_2,i}$  and the mass flow of water vapor  $\dot{m}_{\text{H}_2\text{O},i}$  of each reactor  $i$ . Each reactor can be represented by a detailed chemical reactor model like the one discussed by Grobbel et al. (2022). As this work is based on this model, it is briefly summarized in section 2.2.

To determine valid flux density setpoints for all reactors during operation, a fast reactor model is necessary. Thus, a fast data-driven LSTM neural network is trained in section 2.3 by means of data generated by the detailed thermochemical reactor model. This LSTM model determines the successive temperature and level of ceria reduction of the reactor for a given irradiating flux density.

Section 2.4 describes the receiver controller, which is a hybrid automaton for each reactor. Within the automaton, the LSTM model is embedded to model the continuous state changes. Discrete state changes are executed based on defined rules. In this way, the automaton switches between the redox states and proposes valid flux density setpoints for the next control step that result in high hydrogen production rates.

In section 2.5, heliostat field layout and reactor arrangement are selected. Finally, inner and outer loop are coupled and the cost function used during aim point optimization is defined in section 2.6.

### 2.2. Chemical reactor model

A schematic of the considered solar reactor is shown in figure 2. In its corresponding model, all main components are represented: the quartz window, the porous ceria absorber, the inner housing separating the incoming and leaving gases, the outer housing holding the insulation and the insulation itself. Two coupled, transient, one-dimensional energy transport equations are solved for the solid and fluid phase along the depth of the ceria foam. The chemical reaction of the ceria with the gas phase in the foam is treated by assuming chemical equilibrium between

ceria and the gas for each control volume along the depth of the absorber. Radiation between the components is modeled by view factors; radiation inside the foam with the Beer-Lambert law and with a Rosseland diffusion term in the solid’s energy transport equation. More details about the model can be found in Grobbel et al. (2022).

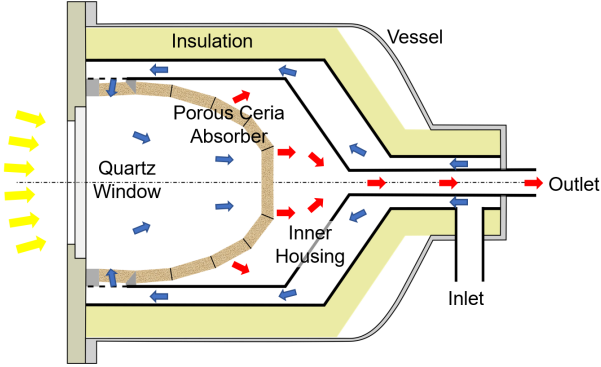


Figure 2: Sectional view of reactor (Grobbel et al., 2022).

From a system control perspective, the model has inputs, states and outputs as shown in figure 3. Within this work, the nitrogen mass flow is set constant to  $75 \text{ kg h}^{-1}$  during the *reduction* step, while the steam flow is set to  $400 \text{ kg h}^{-1}$  during the *oxidation* step. In doing so, the model inputs are reduced to flux density and the type of the reaction step.

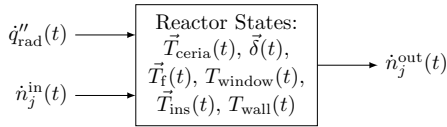


Figure 3: Reactor model from a control system perspective

### 2.3. Long short-term memory neural network model

Various methods exist for time series prediction. Here, the chemical reactor model is transferred to a data-driven one to achieve run time reductions. Popular data-driven methods for time series data are *Autoregressive Integrated Moving Average* (ARIMA) (Box and Pierce, 1970) and *Autoregressive Conditional Heteroscedasticity* (ARCH) (Engle, 1982). Similar to the ARIMA model, artificial neural networks can predict the successive value based on a preceding moving time frame.

Besides the simple *Multilayer Perceptron* (MLP) neural network (Gardner and Dorling, 1998), Hochreiter and Schmidhuber (1997) proposed the concept of LSTM as an artificial *Recurrent Neural Network* (RNN) architecture. There, recurrently connected memory blocks form an LSTM layer. Since Gers et al. (2002) introduced the forget gate, each block comprises memory cell, input, output and forget gate functioning as multipliers for input, output and previous cell value. LSTM neural networks are especially suited for sequence data since they additionally consider the order of the data samples (Duan et al., 2016).

As a physics-driven model is available and enough data can be generated, an LSTM neural network is selected to model a single reactor in this work. As illustrated in figure 4, the LSTM neural network has three input features, each comprising ten inputs, and two outputs. The following features serve as inputs:

- the maximum temperature of the reactor  $T$ ,
- the flux density irradiating onto the reactor  $q''_{\text{rad}}$  and
- the level of ceria reduction  $\delta$ .

Based on these inputs, the model determines the successive temperature change  $\Delta T_{t+1}$  and the successive change in the ceria reduction level  $\Delta \delta_{t+1}$ . Based on these changes, the successive state is determined as presented in equation 3 for the temperature.

$$T_{t+1} = T_t + \Delta T_{t+1} \quad (3)$$

While the flux density  $q''_{\text{rad},t}$  describes the irradiation during the next time step from  $t$  to  $t + 1$ , the other state variables characterize the state at time  $t$ .

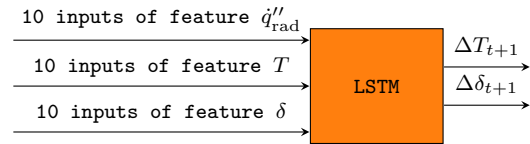


Figure 4: Input features and outputs of the LSTM neural network.

A sequence length of 300 s is chosen as it covers most of the system’s inertia. However, RNNs are trained by *backpropagation through time* (BPTT) (Werbos, 1990). For BPTT long input sequences lead to long training times on the one hand and can result in vanishing or exploding gradients on the other hand (Bengio et al., 1994). As a solution, Williams and Peng (1990) introduced the *truncated backpropagation through time* (TBPTT). There, the BPTT is performed only every  $k_1$  time steps for the preceding  $k_2$  time steps and so the training can be fast, if  $k_2$  is small (Sutskever, 2013). In this work, summarization of the inputs is used as an alternative to counteract the long training times and vanishing or exploding gradients. Hence, the inputs of each feature are not all 300 values from  $t$  to  $t - 299$  s, but

- the mean of the values  $t - 299$  s to  $t - 150$  s,
- the mean of the values  $t - 149$  s to  $t - 50$  s,
- the mean of the values  $t - 49$  s to  $t - 20$  s,
- the mean of the values  $t - 19$  s to  $t - 10$  s,
- the mean of the values  $t - 9$  s to  $t - 6$  s,
- the mean of the values  $t - 5$  s to  $t - 4$  s,
- the value of  $t - 3$  s,
- the value of  $t - 2$  s,
- the value of  $t - 1$  s and
- the value of  $t$ .

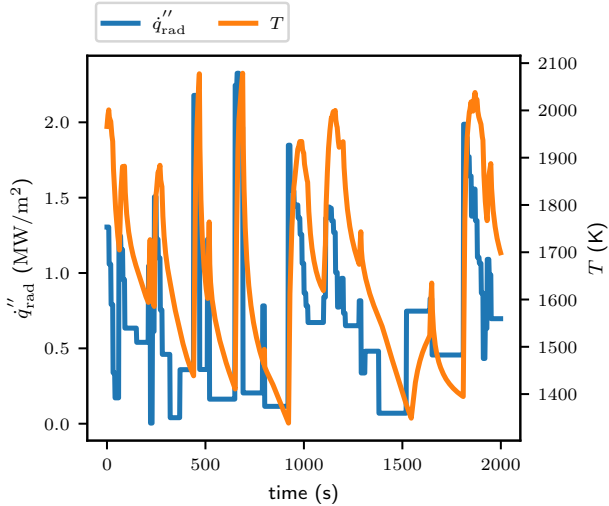


Figure 5: Randomized data generation with the model of Grobber et al. (2022).

As a result, the input size of each feature is reduced from 300 to 10; thus, the training is significantly faster. At the same time, the inputs still represent the system’s inertia, which is relevant to model the time delay in heating and cooling of the reactor.

To form a large enough dataset for the training, the chemical reactor model is simulated for 100 hours. For this, the irradiating flux is varied randomized every ten seconds. If the flux density is below  $750 \text{ kW m}^{-2}$ , the reactor is set to oxidation and otherwise to reduction. Accordingly, the inlet flow is switched from nitrogen to steam and vice versa. Flux densities above  $2250 \text{ kW m}^{-2}$  are not simulated since they are hardly achieved by the evaluated solar tower and do not significantly enhance the reactor’s performance. In addition, the LSTM neural network achieves higher accuracies when its operating range is more confined.

Moreover, some conditions are implemented to reach longer periods of reduction and oxidation. Exemplary, flux densities below  $750 \text{ kW m}^{-2}$  remain constant 85% of the time. In this manner, the reactor achieves its typical toggling behavior visualized in figure 5 for 2000 seconds while being randomized at the same time.

There is no general guideline for the number of layers and memory cells in an LSTM neural network. As enough training data is generated, overfitting is unlikely. Thus, a trade-off between training time and model accuracy is made and two layers with each 20 hidden states are used.

#### 2.4. Receiver controller

Aim of the receiver controller is to determine the next flux density setpoints for the heliostat field control loop. For this, the LSTM model is embedded in a *Hybrid Automaton* (Lunze, 2002). Hybrid automata are well suited to describe dynamic hybrid systems (Henninger, 2000) like the one of the reactor. Here, it consists of four control modes describing heating *Heat*, reduction *Red*, cooling

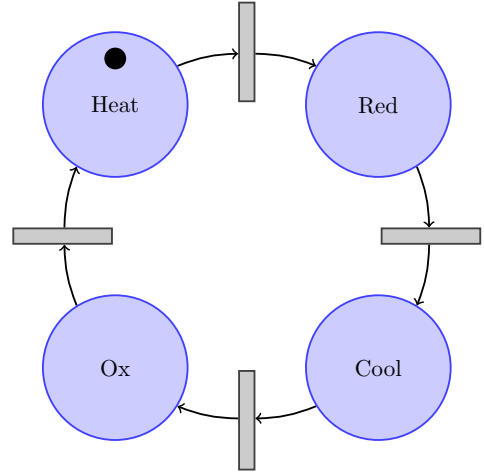


Figure 6: Hybrid automaton comprising the control modes *Heat*, *Red*, *Cool* and *Ox*.

Table 1: Tested flux density input sequences dependent on the control mode and jump conditions of the successive control switches.

Control mode	Flux density input sequences	Jump conditions of control switch
Heat	$\dot{q}''_{\text{rad,max}} = 2.25 \text{ MW m}^{-2}$	$T > 2000 \text{ K}$
Red	$\dot{q}''_{\text{rad,max}} = 2.25 \text{ MW m}^{-2}$ reduce successively by $0.25 \text{ MW m}^{-2}$ , if $T > 2000 \text{ K}$ within P	$\delta > 0.01$ and $t > 50 \text{ s}$ and $\frac{\Delta\delta}{\dot{q}''_{\text{rad}}} < 0.22 \text{ m}^2 \text{ GW}^{-1}$
Cool	$\dot{q}''_{\text{rad}} = 0 \text{ MW m}^{-2}$	$T < 1500 \text{ K}$
Ox	$\dot{q}''_{\text{rad}} = 0 \text{ MW m}^{-2}$	$\delta < 0.002$ or $t > 200 \text{ s}$

*Cool* and oxidation *Ox* as displayed in figure 6. The control modes make the otherwise data-driven model more transparent and the analysis of the control easier.

The reactor is characterized by the actual and the preceding maximum reactor temperatures  $T$ , levels of ceria reduction  $\delta$  and irradiating flux densities  $\dot{q}''_{\text{rad}}$ . An additional state variable is the time  $t$ , which is reinitialized to zero each time a new control mode is activated. Within a control mode, the other state variables are continuously updated by the LSTM model based on the currently irradiating flux density  $\dot{q}''_{\text{rad}}$ .

The thermal controller copies this state of the reactor and simulates the reactor with various flux density input sequences for a prediction horizon of 10 s. The tested flux density input sequences depend on the current control mode and are presented in table 1. Moreover, the jump conditions are listed. The automaton jumps from one control mode to the next if the jump condition of the respective control switch is met. All jump conditions are evaluated based on the state emerging after the prediction horizon.

For fluxes below the maximum allowed flux density of

$\dot{q}_{\text{rad,max}}'' = 2.25 \text{ MW m}^{-2}$ , larger irradiation during heating leads to higher efficiencies. Thus, this is the setpoint of the heliostat field control loop during heating. Higher irradiating flux densities are not modeled as the LSTM neural network is only trained up to this value; thus, it is not valid for higher flux densities.

As soon as the material limit of 2000 K would be exceeded within the prediction horizon when irradiating with  $2.25 \text{ MW m}^{-2}$ , the control mode switches to reduction. During reduction, the flux density is successively reduced. In this way, a high flux density leading to maximum reactor temperatures close to 2000 K within the prediction horizon is identified. Holding the reactor temperatures close to this temperature results in maximum reactor efficiencies while operating the reactor safely at the same time.

Determining the best moment to stop the reduction and start the cooling is more complicated. As first variable, the level of ceria reduction is used since the energy required for heating only pays off, if at least some of the foam is reduced. Moreover, the heat conduction requires some time to heat the foam entirely. Thus, the time is included in the jump condition to provide information about the heating progress. As final decision variable, the reactor efficiency  $\eta_{\text{reactor}}$  as presented in equation 4 should be used.

$$\eta_{\text{reactor}} = \frac{\int \dot{n}_{\text{H}_2}^{\text{out}}(t) dt \cdot \text{HHV}}{\int \dot{q}_{\text{rad}}''(t) dt \cdot A} \quad (4)$$

Here,  $\dot{n}_{\text{H}_2}^{\text{out}}$  is the molar flow of hydrogen, HHV denotes the higher heating value of hydrogen and  $A$  describes the irradiated area.

Hydrogen is only produced during oxidation and the irradiation is mostly required during reduction. Thus, it is impossible to determine the reactor efficiency for a shorter time frame than an entire redox cycle. However, the hydrogen production is proportionally linked to the oxygen that is bonded during oxidation by the foam; thus, it is linked to the change in the level of ceria reduction  $\Delta\delta$  achieved within the previous reduction.  $\Delta\delta$  as well as the irradiation can be quantified for each time frame during the reduction. Thus, the quotient of both is used here as a factor proportional to some kind of current reactor efficiency as expressed in equation 5.

$$\eta_{\text{reactor,current}} \propto f_{\text{reactor,current}} = \frac{\Delta\delta}{\dot{q}_{\text{rad}}''} \quad (5)$$

It provides information on how efficient the energy will be used in this reactor during the next time interval. Hence, this variable is suitable to decide whether the reduction should be pursued. If  $\Delta\delta$  is too small compared to the expended flux density, the energy should better be used in a different reactor. However, as long as this current efficiency is high enough, the reduction is continued. Performing several test runs with different parameter combinations, a value of  $0.22 \text{ m}^2 \text{ GW}^{-1}$  led in

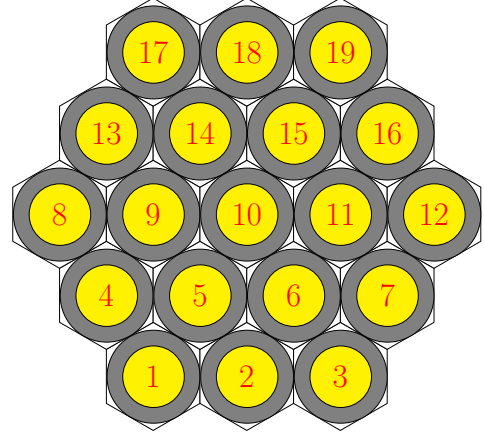


Figure 7: Honeycomb reactor array arrangement.

combination with the other two jump conditions, level of ceria reduction and reduction time, to good results.

During cooling, the reactor should not be irradiated to initiate oxidation as soon as possible and to not consume energy that could be used in heating or reducing reactors instead. Since the foam oxidizes only below maximum reactor temperatures of roughly 1500 K, oxidation starts as soon as the reactor temperature falls below this threshold.

Likewise to cooling, the reactor should not be irradiated during oxidation for the best array efficiency. The reactor remains in oxidation until either the level of ceria reduction falls below a threshold or the reactor is oxidized long enough. In the first case, the foam has oxidized to the point where the reactor would be better off being available for reduction again than oxidizing longer. In the second case, the reactor has difficulty reaching low temperatures due to spillage of heliostats irradiating neighboring reactors. In this case, the oxidation is stopped even though some reduced ceria is left.

### 2.5. Reactor arrangement and heliostat field layout

In previous works like the one of Grobbel et al. (2022), it was assumed that the total power of the heliostat field is constant and that the power can be partitioned as desired to the individual reactors. Here, we want to include the limited concentration capability of the heliostat field. Therefore, an arrangement of multiple reactors is created, in which each reactor has a total diameter of 1 m and a window diameter of 0.662 m, like in the work of Grobbel et al. (2022). To minimize spillage, the reactors are arranged closely in a honeycomb structure as illustrated in figure 7. Additionally, the secondary concentrator described by Buck et al. (2002) is added in front of each reactor. Its radius is also 1 m and the acceptance angle is  $27^\circ$ . Originating from the three reactor case (Säck et al., 2016), an intercepted field power of roughly 5 MW was selected as the next step to commercialization. Moreover, high flux densities are required for the hydrogen production. The diameter of the entire array of reactors is 5 m. As soon

as the heliostat's focal spot exceeds this diameter, spillage is guaranteed. Equation 6 determines the maximum slant range, from which perfectly focusing heliostats cause this size of focal spot just due to the angular diameter of the sun  $\delta_S$ .

$$D_h = \frac{\frac{d}{2}}{\tan \frac{\delta_S}{2}} = \frac{\frac{5 \text{ m}}{2}}{\tan \frac{0.53^\circ}{2}} = 541 \text{ m} \quad (6)$$

As real heliostats show additional errors like mirror or tracking errors, even smaller slant ranges result in radiation onto the whole array of reactors. Even close heliostats radiate onto multiple reactors and the flux cannot be partitioned as desired. Increasing the field power requires heliostats even further away from the receiver; consequently, spillage would increase dramatically.

Based on these considerations, a heliostat field layout with 196 heliostats, each with an area of 36 m<sup>2</sup>, is created by the HFLCAL modeling approach of Schwarzbözl et al. (2009) and visualized in figure 8a. Besides the heliostat position, the optical efficiency  $\eta_{\text{optical}}$  achieved by aiming to the middle reactor, reactor 10, is also visualized. The optical efficiency combines the field losses with the intercept. Thus, it includes spillage, cosine losses, losses due to imperfect reflectivity, atmospheric attenuation, blocking and shading. The layout illustrated in figure 8a delivers 4.9 MW intercepted power with an intercept of 78 % when aiming on the middle reactor of the reactor array. The array is mounted on a 80 m tower and tilted by 25°. The tower is virtually located in Almería, Spain, and the simulations are performed for a DNI of 1000 W m<sup>-2</sup> on 21<sup>st</sup> of March at noon. The high-focus heliostats are simulated with 1 mrad mirror and tracking error, respectively.

19 reactors are chosen according to equation 7 assuming an average flux density of 0.75 MW m<sup>-2</sup> per reactor. Since the 5 MW-field has already 340 m-distant heliostats, larger field sizes are not reasonable without increasing the number of reactors.

$$\begin{aligned} n_{\text{reactors}} &= \frac{Q_{\text{field}}}{\dot{q}_{\text{rad,tru}}'' \pi r_{\text{window}}^2} \\ &= \frac{5 \text{ MW}}{0.75 \text{ MW m}^{-2} \pi (0.331 \text{ m})^2} = 19.36 \end{aligned} \quad (7)$$

For comparison, a second heliostat field is designed that yields the same intercept power onto the reactors without requiring secondary concentrators. As the spillage increases, 383 heliostats are necessary as pictured in figure 8b. However, the maximum distance is reduced to 210 m as the acceptance angle of the secondaries must not be considered any longer and wider fields are possible. The intercept for this heliostat field amounts to 40 %.

## 2.6. Coupling with optical model

The flux density distributions on the reactor array are generated by means of the raytracing software *STRAL*<sup>1</sup>. For this, 19 aim points are defined in the center of each of the 19 reactors, where the heliostats aim to. Within the raytracer, an ant-colony optimization meta-heuristic developed by Belhomme et al. (2013) is embedded as aim point optimization algorithm. Aim point optimization solves the knapsack problem of assigning heliostats to aim points. Thus, it finds aim point configurations leading to flux density distributions close to the best possible ones. The ant-colony optimization uses pre-calculated flux maps and a grouping approach to reduce the simulation time as described by Oberkirsch et al. (2021).

In aim point optimization, the quality of an aim point distribution is evaluated by an objective function  $J$ . The objective function usually maximizes the integrated flux on the receiver  $\mathbf{y}$  while observing the *Allowed Flux Density* (AFD)  $\mathbf{y}_{\text{max}}$ . In this work, the aim is to achieve flux densities closest possible to the desired ones. As objective values between zero and unity are best for the algorithm, a quotient is calculated as presented in equation 8.

$$J(\mathbf{y}) = \frac{\text{num}}{\text{den}} \quad (8)$$

In the numerator, equation 9, the flux densities of the reducing reactors are summed. If the flux density  $y_i$  exceeds the setpoint flux density  $y_{i,\text{set}}$ , nothing is added. In the oxidizing reactors lower flux densities are favored and above 0.75 MW m<sup>-2</sup> hydrogen is hardly produced. Hence, this value is defined as maximum allowed flux density during oxidation  $y_{\text{ox,max}}$ . If the flux density is below this limit, the numerator increases by the difference to this maximum.

$$\begin{aligned} \text{num} &= \sum_i^{n_{\text{reactors,red}}} \begin{cases} y_i, & \text{if } y_i < y_{i,\text{set}} \\ 0, & \text{if } y_i \geq y_{i,\text{set}} \end{cases} \\ &+ \sum_i^{n_{\text{reactors,ox}}} \begin{cases} y_{\text{ox,max}} - y_i, & \text{if } y_i < y_{\text{ox,max}} \\ 0, & \text{if } y_i \geq y_{\text{ox,max}} \end{cases} \\ &\text{and } y_{\text{ox,max}} = 0.75 \text{ MW m}^{-2} \end{aligned} \quad (9)$$

Each term in the denominator, equation 10, has to be larger or equal the numerator to maximally reach unity in the objective function. Thus, the setpoint flux density is added for each reducing reactor if the flux density is below the setpoint and the flux density itself is added if the setpoint is exceeded. For the oxidizing reactors, the denominator rises by the irradiating flux density if it exceeds the maximum allowed flux density during oxidation  $y_{\text{ox,max}}$ . If the flux density is below this limit, the denominator increases by the limit itself.

<sup>1</sup>STRAL is a raytracing software tool developed at the German Aerospace Center (Belhomme et al., 2009).

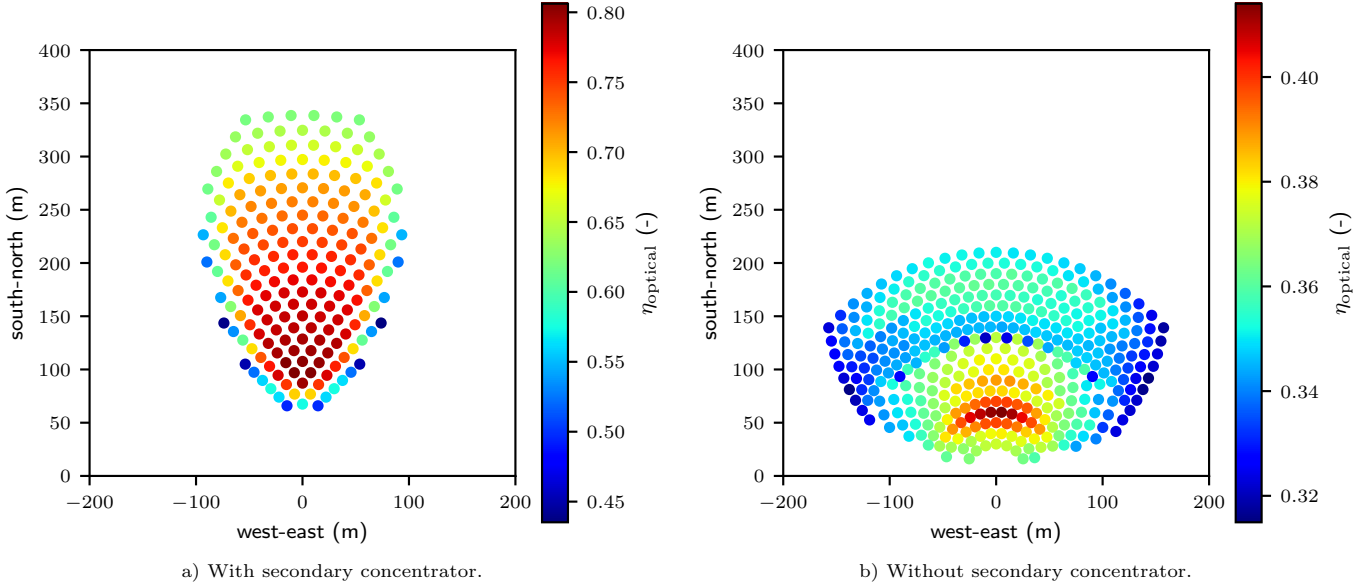


Figure 8: Helioestat field layouts providing 5 MW for receivers with and without secondary concentrators in front of the reactors. The color schema presents the optical efficiency of the individual heliostats.

$$\begin{aligned}
 den = & \sum_i^{n_{\text{reactors,red}}} \begin{cases} y_{i,\text{set}}, & \text{if } y_i < y_{i,\text{set}} \\ y_i, & \text{if } y_i \geq y_{i,\text{set}} \end{cases} \\
 & + \sum_i^{n_{\text{reactors,ox}}} \begin{cases} y_{\text{ox,max}}, & \text{if } y_i < y_{\text{ox,max}} \\ y_i, & \text{if } y_i \geq y_{\text{ox,max}} \end{cases} \\
 & \text{with } y_{\text{ox,max}} = 0.75 \text{ MW m}^{-2} \quad (10)
 \end{aligned}$$

In the ant-colony optimization, an attractiveness is introduced to favor aim points with larger intercept. By means of this, the algorithm automatically shifts the heliostats in the right direction to avoid spillage; consequently, it converges faster. For the application in receivers with multiple thermochemical reactors, the preferred aim points vary depending on the state of the reactors. Aiming to heating up and reducing reactors has to be favored over aiming to cooling or oxidizing reactors. Thus, a new attractiveness matrix is generated automatically prior to each optimization call. If a reactor heats up or reduces, the attractiveness of the corresponding aim point is the setpoint flux density, while the attractiveness of aim points belonging to cooling and oxidizing reactors is zero.

### 3. Results

This section presents the training and testing loss of the LSTM neural network as well as its accuracy and run time. Moreover, an operating sequence of the cascade control for an operation period of 5400 s is shown and the efficiency is determined.

#### 3.1. LSTM model training and testing

For the training, the optimizer *Adaptive Moment Estimation* (ADAM) is applied and the learning rate is succes-

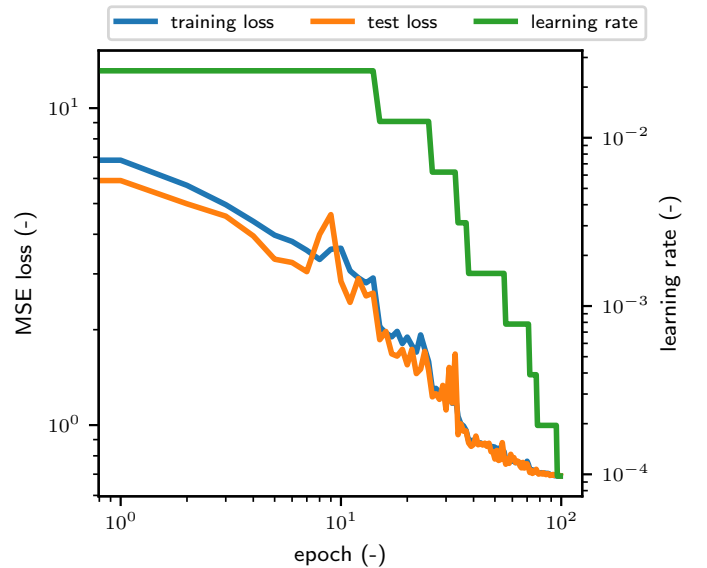


Figure 9: Loss in training and test dataset while training with on plateau reducing learning rate.

sively reduced on plateau starting from 0.05 as visualized in figure 9. With a batch size of 1024, each epoch requires 30 s on an Intel core i5-6300HQ 2.3 GHz quad core processor. In figure 9, training and test loss as well as the learning rate are plotted until the training stops after 100 epochs requiring less than an hour. The convergence of both curves is clearly identifiable.

#### 3.2. Accuracy of LSTM model

In a next step, the data-driven model is compared to the thermochemical model to validate that the accuracy is sufficient for the application in the cascade control. For

this, a cyclic irradiation profile as visualized in the upper half of figure 10 is predefined for both models. Additionally, the arising mole fractions of nitrogen, steam, oxygen and hydrogen are presented. The lower half of the figure presents the courses for the temperature and for the reduction extend. For comparison, the courses for the original thermochemical reactor model and for the LSTM reactor model are plotted. The sharper increase in the reduction extend at the beginning of oxidation is caused by the mass flow rise from  $75 \text{ kg h}^{-1}$  to  $400 \text{ kg h}^{-1}$  while the temperature is too high for oxidation so that the water vapor serves as a purge gas.

In table 2, the *mean absolute error* (MAE), the *root-mean-square error* (RMSE) and the relative error are listed. The data show that the temperature course is fairly simple to grasp, while the level of ceria reduction is more difficult.

Table 2: Errors between chemical and LSTM reactor model.

Variable	MAE	RMSE	relative error
$T$	12.6 K	15.8 K	0.765 %
$\delta$	0.00024	0.00030	1.92 %

### 3.3. Run time of LSTM model

On an Intel core i5-6300HQ 2.3 GHz quad core processor, the run time of the thermochemical model of Grobbel et al. (2022) is roughly fifty times the one of the LSTM model. Though, this thermochemical model is already quite fast as it is only one-dimensional. Hence, training the LSTM neural network with data of more detailed thermochemical models would result in even higher run time reduction ratios.

### 3.4. Simulation analysis

Simulating the thermal controller with secondaries and the jump conditions presented in table 1 for 5400 s results in a control mode sequence plotted in figure 11 for all 19 reactors. Figure 12 presents the setpoint flux density, the achieved flux density, the resulting maximum reactor temperature and the level of ceria reduction during 700 s of operation of reactors 1 and 5. Clearly recognizable is that the individual cycles are shifted to each other.

All reactors are re-simulated by the thermochemical model of Grobbel et al. (2022) using the achieved flux densities determined by the raytracer for each reactor as inputs. In this manner, the reactor efficiencies, equation 4, and the hydrogen production rates of the individual reactors are determined and plotted in figure 13. To minimize the initialization effect, only the last hour of this time frame is evaluated. When the upper and lower half of the circles are compared, it is noticeable that the lower half has a darker red than the upper half in the outer honeycomb ring (reactors: 1, 2, 3, 4, 7, 8, 12, 13, 16, 17, 18, 19), and in the middle honeycomb ring (reactors: 5, 6, 9, 11, 14, 15) the lower half exhibits a lighter red than the upper

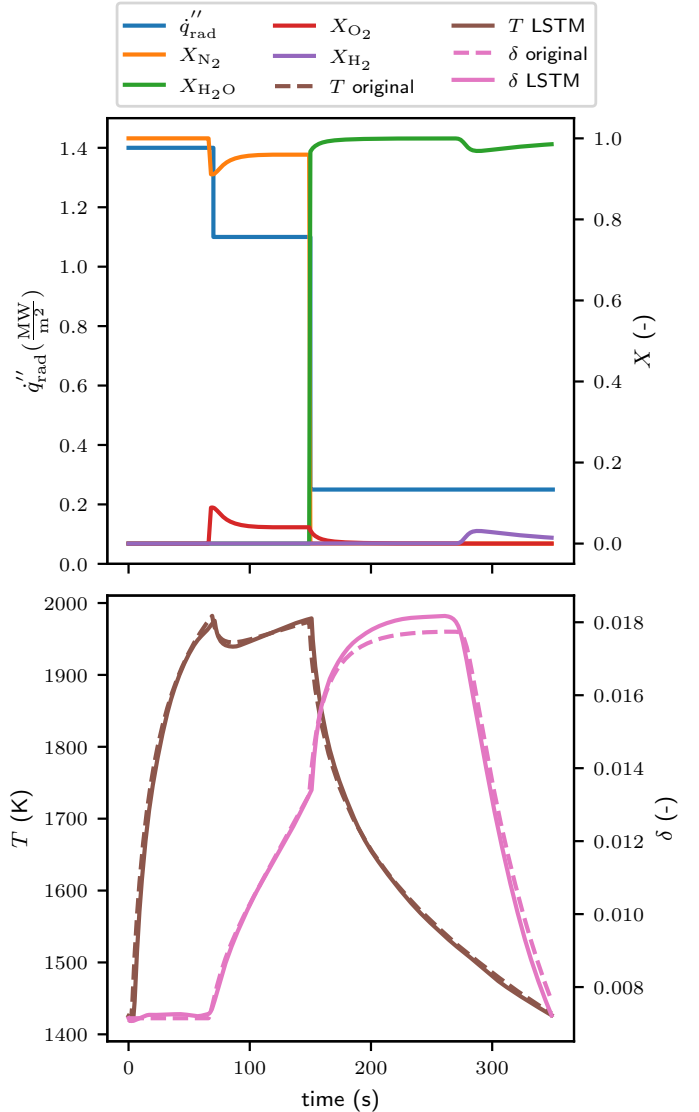


Figure 10: Comparison of original thermochemical and the LSTM reactor model. In the upper half of the figure, the predefined cyclic irradiation profile is plotted. Additionally, the mole fractions of nitrogen, steam, oxygen and hydrogen are presented. In the lower figure half, temperature and level of ceria reduction courses are compared between both models.

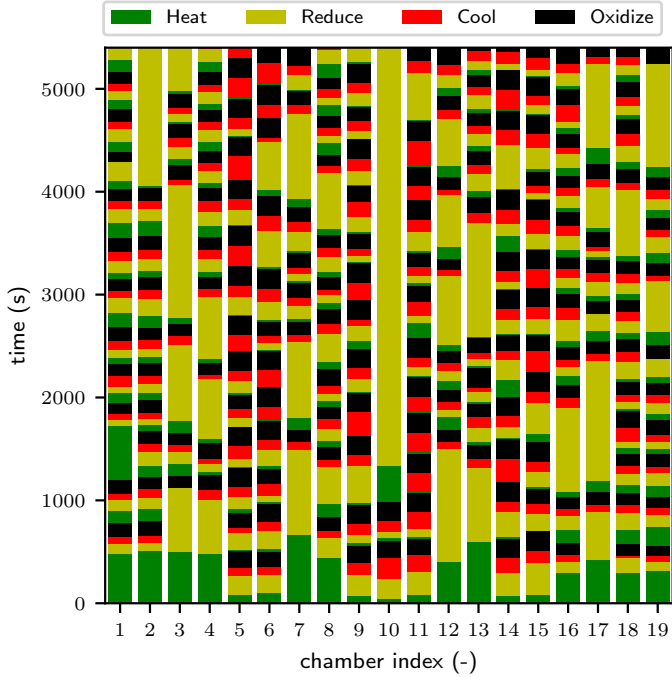


Figure 11: Control modes of the 19 reactors for 1.5 h of operation.

half. The average hydrogen production rate in the middle honeycomb ring is  $28.01 \text{ mmols}^{-1}$ , while the average hydrogen production in the outer ring is  $26.92 \text{ mmols}^{-1}$ . The average reactor efficiency in the mid ring is 3.90%, whereas the reactor efficiency is 4.12% in the outer ring on average. The reason are higher integral fluxes irradiating in the reactors of the middle honeycomb ring causing higher hydrogen production rates but lower reactor efficiencies. The overall reactor efficiency is 3.90% and the overall hydrogen production is 1795 mol.

The maximum allowed temperature is exceeded in 0.8% of the time and the maximum emerging temperature is 2105 K. However, most temperature violations are small as only 0.1% of the time 2020 K are exceeded. In comparison, the simulation without secondary concentrators yields an overall reactor efficiency of 4.68% and an overall hydrogen production of 2305 mol.

### 3.5. Efficiency

The overall efficiency comprises optical efficiency and reactor efficiency. The optimal reactor efficiency is determined by the model of Grobbel et al. (2022). For this, the reduction and oxidation duration are optimized until the optimal reactor efficiency of 5.92% is achieved with a reduction period of 128 s and an oxidation period of 215 s. The average hydrogen production rate is  $42.3 \text{ mmols}^{-1}$  at this point.

The simulation analysis in section 3.4 showed that this optimal reactor efficiency cannot be reached when operating the entire array of reactors. Brendelberger et al. (2020) introduced the term *array efficiency* to quantify this loss. It relates the yield of the whole array to the yield

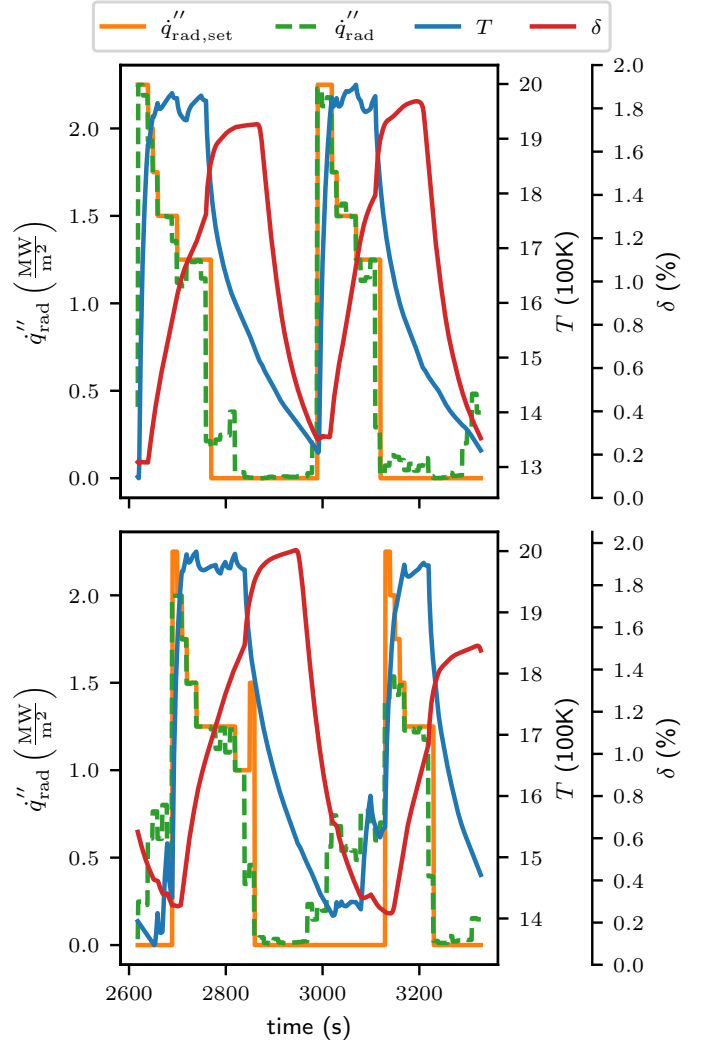


Figure 12: Setpoint flux density, achieved flux density, maximum reactor temperature and level of reduction of reactor 1 (top) and 5 (bottom) during an operation period of 700 s.

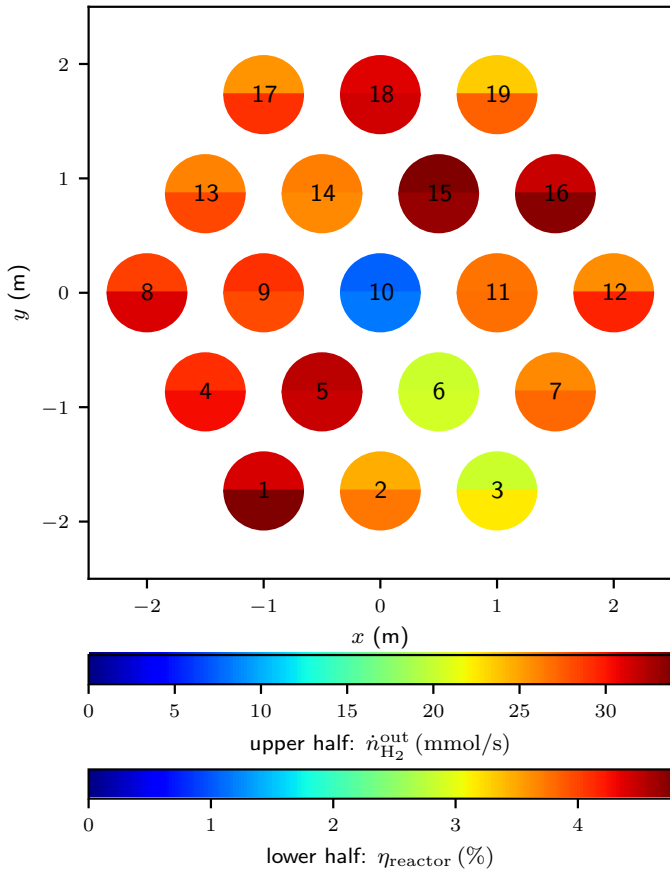


Figure 13: Hydrogen production rates and reactor efficiencies of the 19 reactors.

that would be achieved by freely distributing the flux onto the reactors and by operating each reactor independently. The simulation without secondary concentrators achieves an array efficiency of 79.1%; the field with secondary concentrators an array efficiency of 65.9%.

The optical efficiency is already discussed in section 2.5 for the case when aiming to reactor 10. As soon as heliostats aim to other reactors than the central one, the spillage increases. Due to the increasing spillage, the optical efficiency drops. This performance loss is quantified by a non-centered aiming efficiency  $\eta_{\text{non-centered}}$ . It relates the intercepted energy during operation of all reactors to the intercepted energy when aiming exclusively to the central reactor. It amounts to 80.6% for the case without secondary concentrators and to 75.1% for the case with secondary concentrators.

The array efficiency has to be multiplied with the non-centered aiming efficiency to quantify the total performance loss due the joint operation of the reactors. The product is called combined efficiency and quantified to 49.3% for the simulation with secondary concentrators and to 63.7% for the simulation without.

#### 4. Discussion

This study presented a control for a receiver with multiple reactors for solar thermochemical hydrogen generation. While the receiver exhibits strong dynamics, the heliostat field is assumed static. The developed cascade control takes advantage of this fact and couples heliostat field and receiver control. In contrast to Roca et al. (2016), Säck et al. (2016) and Grobbel et al. (2022), the interdependency between multiple reactors is considered by this control for the first time and 19 batch reactors are operated in parallel by a single solar field. While the periods of oxidation and reduction as well as the temperature setpoints are fixed by Roca et al. (2016) and Säck et al. (2016), they are flexible in this work. Furthermore, variable irradiating fluxes are possible here, whereas they are fixed in the work of Grobbel et al. (2022).

Since a fast receiver model was required for the control, a model based on an LSTM neural network was created. The LSTM neural network's accuracy presented in table 2 is sufficient since temperature deviations of 12.6 K are in the order of other modeling errors. The same applies for the exceedances of the maximum reactor temperature. Furthermore, the reduction extend is only used as criterion in the jump conditions. Thus, a slightly larger error in the modeling of the reduction extend is acceptable.

Figure 11 shows that it is initially most efficient to reduce the seven middle reactors from the optical point of view. However, as soon as the modes of these reactors do not comply anymore, the optimizer decides not to irradiate reactor 10 any longer; thus, it remains in reduction. The reason is that cooling of the honeycomb's mid ring reactors is already challenging and irradiating reactor 10 makes it more complicated. Moreover, the figure illustrates that the

outer ring reactors operate mostly in heating or reduction, while the reactors of the middle ring operate more in cooling or oxidization. The reason is a higher optical efficiency when aiming into more centralized reactors. Consequently, the mid ring reactors have difficulty completing oxidation because they are irradiated too much, while the outer reactors have difficulty completing reduction due to too little irradiation. All in all, this leads to higher hydrogen production rates in the mid ring reactors, while the efficiency is highest in the outer ring reactors as presented in figure 13.

The comparison between the cases with and without secondary concentrators points out that a strong increase in optical efficiency is counteracted by a lower non-centered aiming efficiency and a lower array efficiency. Both efficiencies drop due to further away heliostats creating larger focal spots. These larger focal spots increase the spillage when aiming to non-centered aim points. They also increase the unwanted irradiation of reactors being in oxidation or cooling state if they are next to reactors in reducing or heating state. With larger focal spots, surrounding reactors are affected to a larger extend, which increases the interdependency and complicates the control. Nevertheless, the overall efficiency increases by 51.3% with secondaries due to a significantly higher optical efficiency. To benefit from secondaries and smaller fields at the same time, the individual reactors could be tilted towards each other in the future. In this way, their normal vectors differ and the overall area for heliostat positioning rises.

In their default cases, [Brendelberger et al. \(2020\)](#) states array efficiencies from 52% to 68%. In this work, the simulation achieves array efficiencies of 65.7% with secondary concentrators and 79.0% without. The combined efficiencies are 49.3% and 63.7%. For the comparison, the combined efficiencies are more suited as all heliostats aim to the center of the array of reactors in the default cases of [Brendelberger et al. \(2020\)](#). Unlike [Brendelberger et al. \(2020\)](#), the approach developed here is not limited by a reduction duration that is exactly one-third of the total cycle duration and all reactors can reach the targeted maximum temperature.

To be able to demonstrate the control in an experiment in the very near future, the reactor model used in this study represents an existing solar reactor with all its weaknesses. As the redox foam is planned to be replaced, a 100% ceria content has been assumed in the model, but making other design improvements for this reactor type to increase its efficiency was not the scope of this study and is discussed elsewhere ([Zoller et al., 2019](#); [Brendelberger et al., 2020](#); [Lidor et al., 2021](#)). Concerning the operation investigated in the current study, the combined efficiency can be enhanced by several adaptations:

- The reactors can be tilted to each other to achieve a wider and closer heliostat field with a smaller focal spot.
- In our study, the secondary is only the inner circle of

the hexagon. Aligning the secondaries perfectly can increase the surface by roughly 10%. Consequently, spillage decreases, the field size reduces and the control becomes easier.

- Additional aim points can provide more flexibility for the aim point optimization.
- Instead of adapting only the cost function of the ant-colony optimization, the aim point optimization itself can be adapted.
- The control could benefit from a variable reactor aperture size ([Abedini Najafabadi et al., 2019](#); [Abuseada and Ozalp, 2020](#)) since this would reduce the interdependency between the reactors.

## 5. Conclusion

In this paper, a data-driven model of a solar thermochemical reactor is developed for the efficient control of a receiver with multiple of these reactors. For this, a LSTM neural network is trained with simulation results of a chemical reactor model. It predicts future reactor temperatures based on the preceding reactor state and the irradiating flux with a mean absolute error of 12.6 K. Additionally, the level of ceria reduction is modeled sufficiently accurate to use it as a decision variable for control mode changes of a hybrid automaton. Depending on the control mode, the hybrid automaton determines setpoint flux densities for each reactor that maximize the hydrogen production while observing the material limit of 2000 K. Aim point optimization assigns the heliostats to the reactors to achieve flux density distributions close to these setpoints. In this manner, it maximizes the overall hydrogen production. For an array of reactors without secondary concentrators an array efficiency of 79.0% is achieved. In comparison, the array efficiency drops to 65.7% when including secondary concentrators. However, the overall efficiency increases by 51.3% at the design point as the intercept roughly doubles.

In the future, the overall efficiency should be improved by adapting the field layout, the reactor arrangement, the aim point optimizer and the thermochemical reactor. Furthermore, several control approaches for thermochemical reactors will be demonstrated at the solar tower in Jülich. There, real measurements will be recorded to train the LSTM neural network and to close the control loops.

## 6. Acknowledgement

This work was carried out in the project "H2Loop" (Grant number: EFRE-0801158) with the financial support from the Ministry of Economic Affairs, Innovation, Digitalization and Energy of the State of North Rhine-Westphalia.

## References

- International Energy Agency, The Future of Hydrogen, 2019. URL: <https://www.oecd-ilibrary.org/content/publication/1e0514c4-en>. doi:<https://doi.org/https://doi.org/10.1787/1e0514c4-en>.
- T. Nakamura, Hydrogen production from water utilizing solar heat at high temperatures, *Solar Energy* 19 (1977) 467–475. URL: <https://www.sciencedirect.com/science/article/pii/S0038092X77901025>. doi:[https://doi.org/10.1016/0038-092X\(77\)90102-5](https://doi.org/10.1016/0038-092X(77)90102-5).
- M. Roeb, J. P. Säck, P. Rietbrock, C. Prah, H. Schreiber, M. Neises, L. de Oliveira, D. Graf, M. Ebert, W. Reinalter, M. Meyer-Grünefeldt, C. Sattler, A. Lopez, A. Vidal, A. Elsberg, P. Stobbe, D. Jones, A. Steele, S. Lorentzou, C. Pagkoura, A. Zygogianni, C. Agrafiotis, A. G. Konstandopoulos, Test operation of a 100 kW pilot plant for solar hydrogen production from water on a solar tower, *Solar Energy* 85 (2011) 634–644. URL: <https://www.sciencedirect.com/science/article/pii/S0038092X10001623>. doi:<https://doi.org/10.1016/j.solener.2010.04.014>.
- I. Ermanoski, N. P. Siegel, E. B. Stechel, A new reactor concept for efficient solar-thermochemical fuel production, *Journal of Solar Energy Engineering* 135 (2013) 031002. URL: <https://doi.org/10.1115/1.4023356>. doi:[10.1115/1.4023356](https://doi.org/10.1115/1.4023356).
- A. Singh, J. Lapp, J. Grobbel, S. Brendelberger, J. P. Reinhold, L. Olivera, I. Ermanoski, N. P. Siegel, A. McDaniel, M. Roeb, C. Sattler, Design of a pilot scale directly irradiated, high temperature, and low pressure moving particle cavity chamber for metal oxide reduction, *Solar Energy* 157 (2017) 365–376. doi:[10.1016/j.solener.2017.08.040](https://doi.org/10.1016/j.solener.2017.08.040).
- D. Marxer, P. Furler, M. Takacs, A. Steinfeld, Solar thermochemical splitting of CO<sub>2</sub> into separate streams of CO and O<sub>2</sub> with high selectivity, stability, conversion, and efficiency, *Energy Environ. Sci.* 10 (2017) 1142–1149. URL: <http://dx.doi.org/10.1039/C6EE03776C>. doi:[10.1039/C6EE03776C](https://doi.org/10.1039/C6EE03776C).
- C. Agrafiotis, M. Roeb, C. Sattler, A review on solar thermal syngas production via redox pair-based water/carbon dioxide splitting thermochemical cycles, *Renewable and Sustainable Energy Reviews* 42 (2015) 254–285. URL: <https://ideas.repec.org/a/eee/rensus/v42y2015cp254-285.html>. doi:[10.1016/j.rser.2014.09.03](https://doi.org/10.1016/j.rser.2014.09.03).
- R. B. Diver, J. E. Miller, N. P. Siegel, T. A. Moss, Testing of a CR5 solar thermochemical heat engine prototype, *ASME*, May 17–22, 2010, pp. 97–104. doi:[10.1115/ES2010-90093](https://doi.org/10.1115/ES2010-90093).
- C. P. Falter, A. Sizmann, R. Pitz-Paal, Modular reactor model for the solar thermochemical production of syngas incorporating counter-flow solid heat exchange, *Solar Energy* 122 (2015) 1296–1308. doi:[10.1016/j.solener.2015.10.042](https://doi.org/10.1016/j.solener.2015.10.042).
- S. Brendelberger, P. Holzemer-Zerhusen, E. Vega Puga, M. Roeb, C. Sattler, Study of a new receiver-reactor cavity system with multiple mobile redox units for solar thermochemical water splitting, *Solar Energy* 235 (2022) 118–128. URL: <https://www.sciencedirect.com/science/article/pii/S0038092X22001104>. doi:[10.1016/j.solener.2022.02.013](https://doi.org/10.1016/j.solener.2022.02.013).
- J.-P. Säck, S. Breuer, P. Cotelli, A. Houaijia, M. Lange, M. Wullenkord, C. Spenke, M. Roeb, C. Sattler, High temperature hydrogen production: Design of a 750KW demonstration plant for a two step thermochemical cycle, *Solar Energy* 135 (2016) 232–241. doi:[10.1016/j.solener.2016.05.059](https://doi.org/10.1016/j.solener.2016.05.059).
- S. Yang, L. Li, B. Wang, S. Li, J. Wang, P. Lund, W. Lipiński, Thermodynamic analysis of a conceptual fixed-bed solar thermochemical cavity receiver-reactor array for water splitting via ceria redox cycling, *Frontiers in Energy Research* 9 (2021). URL: <https://www.frontiersin.org/article/10.3389/fenrg.2021.565761>.
- L. Roca, A. de La Calle, L. J. Yebra, Heliostat-field gain-scheduling control applied to a two-step solar hydrogen production plant, *Applied Energy* 103 (2013) 298–305. doi:[10.1016/j.apenergy.2012.09.047](https://doi.org/10.1016/j.apenergy.2012.09.047).
- J.-P. Säck, M. Roeb, C. Sattler, R. Pitz-Paal, A. Heinzl, Development of a simulation-software for a hydrogen production process on a solar tower, *Solar Energy* 112 (2015) 205–217. URL: <https://www.sciencedirect.com/science/article/pii/S0038092X14005702>. doi:[10.1016/j.solener.2014.11.026](https://doi.org/10.1016/j.solener.2014.11.026).
- L. Roca, R. Diaz-Franco, A. de La Calle, J. Bonilla, A. Vidal, A control based on a knapsack problem for solar hydrogen production, *Optimal Control Applications and Methods* 37 (2016) 496–507. doi:[10.1002/oca.2118](https://doi.org/10.1002/oca.2118).
- L. Li, Y. Li, H. Yu, Y.-L. He, A feedforward-feedback hybrid control strategy towards ordered utilization of concentrating solar energy, *Renewable Energy* 154 (2020a) 305–315. URL: <https://www.sciencedirect.com/science/article/pii/S0960148120303189>. doi:[10.1016/j.renene.2020.03.004](https://doi.org/10.1016/j.renene.2020.03.004).
- L. Li, S. Yang, B. Wang, J. Pye, W. Lipiński, Optical analysis of a solar thermochemical system with a rotating tower reflector and a receiver-reactor array, *Opt. Express* 28 (2020b) 19429–19445. URL: <http://opg.optica.org/oe/abstract.cfm?URI=oe-28-13-19429>. doi:[10.1364/OE.389924](https://doi.org/10.1364/OE.389924).
- R. Schächli, D. Rutz, F. Dähler, A. Muroyama, P. Haueter, J. Lilliestam, A. Patt, P. Furler, A. Steinfeld, Drop-in fuels from sunlight and air, *Nature* 601 (2022) 63–68. doi:<https://doi.org/10.1038/s41586-021-04174-y>.
- S. Brendelberger, A. Rosenstiel, A. Lopez-Roman, C. Prieto, C. Sattler, Performance analysis of operational strategies for monolithic receiver-reactor arrays in solar thermochemical hydrogen production plants, *International Journal of Hydrogen Energy* 45 (2020) 26104–26116. doi:<https://doi.org/10.1016/j.ijhydene.2020.06.191>.
- J. Grobbel, M. F. Sollich, D. M. Quinto, A. Lidor, C. Sattler, Operation optimization of an array of receiver-reactors for solar fuel production, *AIP Conference Proceedings* 2445 (2022) 130004. URL: <https://aip.scitation.org/doi/abs/10.1063/5.0085738>. doi:[10.1063/5.0085738](https://doi.org/10.1063/5.0085738). arXiv:<https://aip.scitation.org/doi/pdf/10.1063/5.0085738>.
- J. A. Carballo, J. Bonilla, M. Berenguel, J. Fernández-Reche, G. García, New approach for solar tracking systems based on computer vision, low cost hardware and deep learning, *Renewable Energy* 133 (2019) 1158–1166. URL: <https://www.sciencedirect.com/science/article/pii/S0960148118310516>. doi:<https://doi.org/10.1016/j.renene.2018.08.101>.
- J. A. Carballo, J. Bonilla, M. Berenguel, J. Fernández, G. García, Solar tower power mockup for the assessment of advanced control techniques, *Renewable Energy* 149 (2020) 682–690. URL: <https://www.sciencedirect.com/science/article/pii/S0960148119319470>. doi:<https://doi.org/10.1016/j.renene.2019.12.075>.
- M. Pargmann, D. Maldonado Quinto, P. Schwarzbözl, R. Pitz-Paal, High accuracy data-driven heliostat calibration and state prediction with pretrained deep neural networks, *Solar Energy* 218 (2021) 48–56. URL: <https://www.sciencedirect.com/science/article/pii/S0038092X21000621>. doi:<https://doi.org/10.1016/j.solener.2021.01.046>.
- J. Wang, L. Guo, C. Zhang, L. Song, J. Duan, L. Duan, Thermal power forecasting of solar power tower system by combining mechanism modeling and deep learning method, *Energy* 208 (2020) 118403. URL: <https://www.sciencedirect.com/science/article/pii/S0360544220315103>. doi:<https://doi.org/10.1016/j.energy.2020.118403>.
- Z. Zeng, D. Ni, G. Xiao, Real-time heliostat field aiming strategy optimization based on reinforcement learning, *Applied Energy* 307 (2022) 118224. URL: <https://www.sciencedirect.com/science/article/pii/S0360261921014896>. doi:<https://doi.org/10.1016/j.apenergy.2021.118224>.
- G. E. Box, D. A. Pierce, Distribution of residual autocorrelations in autoregressive-integrated moving average time series models, *Journal of the American Statistical Association* 65 (1970) 1509–1526. doi:<https://doi.org/10.2307/2284333>.
- R. F. Engle, Autoregressive conditional heteroscedasticity with estimates of the variance of united kingdom inflation, *Econometrica* 50 (1982) 987–1007. URL: <http://www.jstor.org/stable/1912773>. doi:<https://doi.org/10.2307/1912773>.
- M. Gardner, S. Dorling, Artificial neural networks (the multi-

- layer perceptron)—a review of applications in the atmospheric sciences, *Atmospheric Environment* 32 (1998) 2627–2636. URL: <https://www.sciencedirect.com/science/article/pii/S1352231097004470>. doi:[https://doi.org/10.1016/S1352-2310\(97\)00447-0](https://doi.org/10.1016/S1352-2310(97)00447-0).
- S. Hochreiter, J. Schmidhuber, Long Short-Term Memory, *Neural computation* 9 (1997) 1735–1780. doi:<https://doi.org/10.1162/neco.1997.9.8.1735>.
- F. A. Gers, N. N. Schraudolph, J. Schmidhuber, Learning precise timing with LSTM recurrent networks, *Journal of machine learning research* 3 (2002) 115–143. doi:<https://doi.org/10.1162/153244303768966139>.
- Y. Duan, Y. L.V., F.-Y. Wang, Travel time prediction with LSTM neural network, in: 2016 IEEE 19th International Conference on Intelligent Transportation Systems (ITSC), 2016, pp. 1053–1058. doi:[10.1109/ITSC.2016.7795686](https://doi.org/10.1109/ITSC.2016.7795686).
- P. Werbos, Backpropagation through time: what it does and how to do it, *Proceedings of the IEEE* 78 (1990) 1550–1560. doi:[10.1109/5.58337](https://doi.org/10.1109/5.58337).
- Y. Bengio, P. Simard, P. Frasconi, Learning long-term dependencies with gradient descent is difficult, *IEEE Transactions on Neural Networks* 5 (1994) 157–166. doi:[10.1109/72.279181](https://doi.org/10.1109/72.279181).
- R. J. Williams, J. Peng, An Efficient Gradient-Based Algorithm for On-Line Training of Recurrent Network Trajectories, *Neural Computation* 2 (1990) 490–501. URL: <https://doi.org/10.1162/neco.1990.2.4.490>. doi:[10.1162/neco.1990.2.4.490](https://doi.org/10.1162/neco.1990.2.4.490).
- I. Sutskever, Training recurrent neural networks, Ph.D. thesis, 2013. URL: [https://www.cs.utoronto.ca/~ilya/pubs/ilya\\_sutskever\\_phd\\_thesis.pdf](https://www.cs.utoronto.ca/~ilya/pubs/ilya_sutskever_phd_thesis.pdf).
- J. Lunze, What Is a Hybrid System?, in: S. Engell, G. Frehse, E. Schnieder (Eds.), *Modelling, Analysis, and Design of Hybrid Systems*, Springer Berlin Heidelberg, Berlin, Heidelberg, 2002, pp. 3–14. doi:[10.1007/3-540-45426-8\\_1](https://doi.org/10.1007/3-540-45426-8_1).
- T. A. Henzinger, *The Theory of Hybrid Automata*, Springer Berlin Heidelberg, Berlin, Heidelberg, 2000, pp. 265–292. URL: [https://doi.org/10.1007/978-3-642-59615-5\\_13](https://doi.org/10.1007/978-3-642-59615-5_13). doi:[10.1007/978-3-642-59615-5\\_13](https://doi.org/10.1007/978-3-642-59615-5_13).
- R. Buck, T. Bräuning, T. Denk, M. Pfänder, F. Schwarzbözl, Peter Tellez, Solar-hybrid gas turbine-based power tower systems (REFOS), *Journal of Solar Energy Engineering* 124 (2002). URL: <https://doi.org/10.1115/1.1445444>. doi:[10.1115/1.1445444](https://doi.org/10.1115/1.1445444).
- P. Schwarzbözl, R. Pitz-Paal, M. Schmitz, Visual HFLCAL - A Software Tool for Layout and Optimisation of Heliostat Fields, in: T. Mancini, R. Pitz-Paal (Eds.), *SolarPACES 2009*, 2009. URL: <https://elib.dlr.de/60308/>.
- B. Belhomme, R. Pitz-Paal, P. Schwarzbözl, S. Ulmer, A New Fast Ray Tracing Tool for High-Precision Simulation of Heliostat Fields, *Journal of Solar Energy Engineering* 131 (2009). URL: <https://doi.org/10.1115/1.3139139>. doi:[10.1115/1.3139139](https://doi.org/10.1115/1.3139139).
- B. Belhomme, R. Pitz-Paal, P. Schwarzbözl, Optimization of Heliostat Aim Point Selection for Central Receiver Systems Based on the Ant Colony Optimization Metaheuristic, *Journal of Solar Energy Engineering* 136 (2013). URL: <https://doi.org/10.1115/1.4024738>. doi:[10.1115/1.4024738](https://doi.org/10.1115/1.4024738).
- L. Oberkirsch, D. Maldonado Quinto, P. Schwarzbözl, B. Hoffschmidt, GPU-based aim point optimization for solar tower power plants, *Solar Energy* (2021). URL: <https://www.sciencedirect.com/science/article/pii/S0038092X20312123>. doi:<https://doi.org/10.1016/j.solener.2020.11.053>.
- S. Zoller, E. Koepf, P. Roos, A. Steinfeld, Heat Transfer Model of a 50 kW Solar Receiver-Reactor for Thermochemical Redox Cycling Using Cerium Dioxide, *Journal of Solar Energy Engineering, Transactions of the ASME* 141 (2019). URL: <https://www.scopus.com/inward/record.uri?eid=2-s2.0-85059944643&doi=10.1115%2f1.4042059&partnerID=40&md5=159cac31ccaad29f300c528c93e1a87c>. doi:[10.1115/1.4042059](https://doi.org/10.1115/1.4042059).
- A. Lidor, T. Fend, M. Roeb, C. Sattler, High performance solar receiver-reactor for hydrogen generation, *Renewable Energy* 179 (2021) 1217–1232. URL: <https://www.sciencedirect.com/science/article/pii/S0960148121010946>. doi:<https://doi.org/10.1016/j.renene.2021.07.089>.
- H. Abedini Najafabadi, N. Ozalp, C. Ophoff, D. Moens, An experimental study on temperature control of a solar receiver under transient solar load, *Solar Energy* 186 (2019) 52–59. URL: <https://www.sciencedirect.com/science/article/pii/S0038092X19304475>. doi:[10.1016/j.solener.2019.05.002](https://doi.org/10.1016/j.solener.2019.05.002).
- M. Abuseada, N. Ozalp, Experimental and numerical study on heat transfer driven dynamics and control of transient variations in a solar receiver, *Solar Energy* 211 (2020) 700–711. URL: <https://www.sciencedirect.com/science/article/pii/S0038092X20310628>. doi:[10.1016/j.solener.2020.10.009](https://doi.org/10.1016/j.solener.2020.10.009).